Received: 11 January 2024 | Accepted: 28 May 2024

DOI: 10.1111/1365-2478.13556

Geophysical Prospecting EAGE EUROPEAN ASSOCIATION OF GEOSCIENTISTS & ENGINEERS

ORIGINAL ARTICLE

# Processing of unmanned underwater vehicle vector magnetometer data

**J.-F. Oehler**[1] | **V. Schifano**[2] | **G. Marquis**[2] | **H. Reiller**[2] | **S. Lucas**[1] | **C. Bougeault**[1]

[1]Shom, Brest, France

[2]ITES, UMR 7063 University of Strasbourg/CNRS/ENGEES, Strasbourg, France

**Correspondence**
J.-F. Oehler, Shom, 13 rue du Châtellier, CS 92803, 29228 Brest, France.
Email: jean-francois.oehler@shom.fr

**Present address**
H. Reiller, IRD, 101 Promenade Roger Laroque, 98848 Nouméa, Nouvelle-Calédonie, France.

Paper presented at the 84th EAGE Annual Conference & Exhibition, Vienna, Austria

**Funding information**
Defence Innovation Agency (DIA), French Defence Procurement Agency (DGA), French Ministry for Armed Forces

**Abstract**

Marine magnetometry very close to the targeted sources, even in very deep waters, is today a reality with the advent of autonomous underwater vehicles. We argue that a successful approach is to fully integrate the magnetometer onboard the autonomous underwater vehicle and to deal with its static magnetic noise, that is induced and permanent fields of the drone, with a 3-axis vector measurement of the Earth's magnetic field. This argument is supported by results from three magnetic surveys performed with different fluxgate magnetic sensors embedded in autonomous underwater vehicles of increasing sizes. They show that simple specifically defined figures of merit coupled to an optimized scalar calibration procedure derived from aeromagnetic and satellite-borne developments produce reliable magnetic measurements from autonomous underwater vehicles for geophysical mapping or detection applications. Results are impressive and show that even weak magnetic anomalies smaller than 10 nT can be highlighted even though the magnetic signatures of autonomous underwater vehicles can be orders of magnitude higher.

**KEYWORDS**
data processing, magnetics, modelling, potential field

## INTRODUCTION

Marine magnetic surveys have been in use for a long time for various applications that range from marine geological studies to the offshore detection of anthropogenic objects. Traditionally, most marine magnetic surveys are performed using towed scalar sensors to reduce the effects of the massive steel ship on the magnetic measurements. In addition to its navigational constraints and positioning issues, this approach has obvious limitations in spatial resolution when surveying over increasing depths, as the field from the sources generally decreases with distance.

The advent of autonomous underwater vehicles (AUV) offers new opportunities in marine geophysics by allowing fully programmed, automatic surveys and by bringing the magnetic measurements closer to the targeted sources, even in very deep waters. These vehicles have, however, their own electromagnetic signatures that can also pollute the magnetic measurements. Then, specific technical assemblies, careful integration studies of magnetic sensors and/or appropriate mitigations are often mandatory to converge to uncorrupted geophysical measurements.

At least three different technical methods of performing magnetometry from AUVs are documented in the literature:

- Some authors follow surveying from surface vessels by towing 'fish-type' instruments with AUVs. They choose to avoid the magnetic noise by towing scalar Overhauser magnetometers at a distance of a few metres behind the AUV where no interferences are noticeable (e.g. Dhanak et al., 2013; Teixeira et al., 2016; Tilley et al., 2012).
- Other teams opt to mount the magnetic sensor a few metres away from the AUV to reduce its effects. For example, Seidel et al. (2023) rigidly attached three submersible vector fluxgate magnetometers, at a lateral distance of 2 m, to the nose of a Girona 500 AUV, that is far enough from the rear thrusters that are considered the main source of carrier noise. However, this precaution does not prevent a relatively significant induced error mainly related to the heading of the AUV. The authors do not give any details on how it was corrected, apart from acquiring Figure 8 calibration measurements. They focus on the noise of the AUV related to thruster activity that they remove by applying a low-pass Butterworth filter. Wang et al. (2023) connected a magnetic anomaly detection system behind an AUV with two scalar and one vector magnetometers deployed on a rigid frame. They propose a comprehensive compensation model of the induced and permanent fields of the drone to correct for its magnetic interferences.
- Embedded systems are the last alternative to work with, but they require to deal with the signature of the drone itself. Most works document the full integration of 3-axis fluxgate magnetometers in AUVs. In the 1990s, Tivey et al. (1998) studied submarine lava flows in the Juan de Fuca Ridge with the 'Autonomous Benthic Explorer' (known as ABE). They, however, do not provide any details on how they processed their magnetic data. In any case, perturbations due to their AUV were likely not an issue as the objects investigated, such as volcanic areas in the context of mid-oceanic ridges, produced anomalies of thousands of nanoTeslas (nT). Honsho et al. (2013) and Kasaya et al. (2023) also equipped JAMSTEC's AUVs with vector magnetometers. Both groups applied the correction method developed by Isezaki (1986) for the shipboard three-component magnetometer (STCM) to reduce the magnetic field produced by the AUVs themselves. Bloomer et al. (2014) validated a proof of concept during a survey with two 3-axis fluxgate sensors in the nose cone section of an Explorer Class AUV. They defined a calibration manoeuvre to be done prior to every survey to remove the effects of the magnetic field of the drone. The AUV has to navigate following two sequential coincident squares in an area small enough to avoid variations of the local ambient magnetic field. Calibration data are then used to compute correction terms to remove the influence of the AUV. Guo et al. (2022) more recently proposed an adaptative calibration of the rotation error of total magnetic field for AUV based on the Marine Predators Algorithm (Faramarzi et al., 2020) and tested it on outdoor pool test and sea trials data acquired with three-component magnetometers. Berrios-Rivera et al. (2023) deployed the sensor near the top of the Sentry AUV. They performed specific navigation spins before each dive that were used to determine calibration coefficients from best fitting sinusoids and correct azimuth-dependent variations due to the induced and permanent fields of the vehicle. On the opposite, Gallimore et al. (2020) attached the scalar Micro-Fabricated Atomic Magnetometer (MFAM) to the nose of a small REMUS 100. They compensated interferences from the AUV platform by applying an empirical heading error correction and a low-pass filter to attenuate the significant magnetic noise due to the proximity of electrical motors.

Mainly for the operational matter of easing the navigational control of the AUV, we argue in this paper that the best option is to fully integrate the magnetometer onboard the AUV and to deal with its static magnetic noise with a 3-axis vector measurement of the Earth's magnetic field. We support our argument by presenting results from three magnetic surveys performed with different fluxgate magnetic sensors embedded in AUVs of increasing sizes. We emphasize, following Bloomer et al. (2014) and Kasaya et al. (2023), that an appropriate reduction of induced and permanent fields of the drone itself, because of its attitude and especially its changes in heading, pitch and roll, is indispensable to optimize the measurement of small-scaled magnetic anomalies. We finally defend that simple, specifically defined manoeuvres coupled to an optimized scalar calibration procedure derived from aeromagnetic and satellite-borne developments (Munschy et al., 2007; Olsen et al., 2003) produce reliable magnetic measurements from AUVs for geophysical mapping or detection applications.

## THEORETICAL BACKGROUND

Vector fluxgate magnetometers come with three types of inner defects that impact their measurements (Primdahl et al., 1979):

- Each of the three sensor probes has its own sensitivity, which generally drifts over time and depends on the ambient temperature.
- Each probe, placed in a zero ambient field, measures a weak non-zero magnetic field due to the electronic components and ferromagnetic compounds which constitute and surround it; this is what we define as the offset.
- The probes are orthogonally arranged in order to measure the magnetic field in the three directions. The accuracy of

the magnetic intensity deduced from the three components of the field therefore depends directly on the orthogonality of the probes.

The direct output measurement of the magnetic field obtained with a vector fluxgate sensor is thus marred by these problems of sensitivity, offset and non-orthogonality. In order to achieve some high-precision measurements to characterize small-scale magnetic anomalies, the raw sensor data must be carefully calibrated to correct them and obtain the actual value of the Earth's magnetic field.

The principle of scalar calibration is to reset the measurement of the intensity at the sensor output to a reference value, that is either modelled or accurately measured in the vicinity. However, in addition to the inner defects mentioned above, the environment where the sensor is measuring is systematically disturbed magnetically. These parasite fields can range from a few hundred nT to several thousand nT depending on the context and on the carrier. For spatial applications, Olsen et al. (2003) presented a scalar calibration method based on the identification and correction of the nine sensor defects. The assumption made and demonstrated later by Munschy et al. (2007) is that the sensor measures at the same time the local magnetic field along with the magnetic footprint of the carrier and the imperfections of the sensor. Moreover, for data acquired by varying the sensor orientation in a constant magnetic field, the only variations observed between the (supposedly) known intensity of this field and the intensities obtained with the fluxgate are due to the magnetic footprint of the carrier and the sensors' imperfections.

Mathematically, it is thus possible to reduce all the perturbations above in only nine parameters of offset, sensitivity and non-orthogonality that are then used to correct the raw data. Summarizing the scalar calibration of Olsen et al. (2003), we express the sensor output measurement $\mathbf{H}_{\text{mes}} = (H^x_{\text{mes}},\ H^y_{\text{mes}},\ H^z_{\text{mes}})^{\text{T}}$ in the sensor coordinate system, as a function of the ambient magnetic field considered here as the regional magnetic field $\mathbf{H}_{\text{earth}} = (H^x_{\text{earth}},\ H^y_{\text{earth}},\ H^z_{\text{earth}})^{\text{T}}$ as

$$\mathbf{H}_{\text{mes}} = \mathbf{S} \cdot \mathbf{P} \cdot \mathbf{H}_{\text{earth}} + \mathbf{O}, \tag{1}$$

with $\mathbf{S}$ the matrix of the three components sensitivities such that

$$\mathbf{S} = \begin{pmatrix} S_1 & 0 & 0 \\ 0 & S_2 & 0 \\ 0 & 0 & S_3 \end{pmatrix},$$

where $\mathbf{P}$ is the rotation matrix of a vector from an orthogonal coordinate system to the coordinate system of the sensor such that

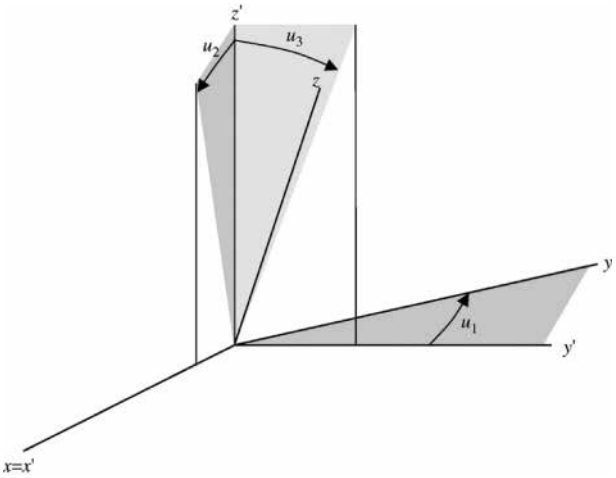


**FIGURE 1** Definition of the angles allowing the transformation from the non-orthogonal coordinate system of the sensor ($x'$, $y'$, $z'$) to the orthogonal coordinate system of the Earth's magnetic field ($x$, $y$, $z$). *Source*: From Munschy et al. (2007).

$$\mathbf{P} = \begin{pmatrix} 1 & 0 & 0 \\ -\sin u_1 & \cos u_1 & 0 \\ \sin u_2 & \sin u_3 & \sqrt{\left(1 - \sin^2 u_1 - \sin^2 u_3\right)} \end{pmatrix},$$

where $u_1$, $u_2$ and $u_3$ are the angles defined in Figure 1, and $O$ represents the offset for each probe such that $\mathbf{O} = (O_1,\ O_2,\ O_3)^{\text{T}}$.

Following Olsen et al. (2003), we use a classical least-squares approach to estimate the nine correction parameters by minimizing the difference between the reference magnetic field intensity and the measured one. The objective function $\varphi$ to minimize is as follows:

$$\varphi = \sum_{i=1}^{N} \left( \|\mathbf{H}_{\text{earth}}\| - \|\mathbf{H}_{\text{mes}}\| \right)^2, \tag{2}$$

and the International Geomagnetic Reference Field (Alken et al, 2021) is chosen as reference for the regional magnetic field $\mathbf{H}_{\text{earth}}$. This inverse problem is stable and converges rapidly.

Once the elements of matrices $\mathbf{S}$, $\mathbf{P}$ and $\mathbf{O}$ and of vector O have been determined, they are applied to the raw data to compute a corrected, calibrated scalar magnetic field $\mathbf{H}_{\text{cal}}$:

$$\mathbf{H}_{\text{cal}} = \sqrt{\left[\mathbf{P}^{-1}\mathbf{S}^{-1}\left(\mathbf{H}_{\text{mes}} - \mathbf{O}\right)\right]^{\text{T}} \left[\mathbf{P}^{-1}\mathbf{S}^{-1}\left(\mathbf{H}_{\text{mes}} - \mathbf{O}\right)\right]} \tag{3}$$

This field is referred to as the calibrated field in the remainder of this paper. The inverse matrices $\mathbf{P}^{-1}$ and $\mathbf{S}^{-1}$ are already detailed by Olsen et al. (2003).

However, for this method to be efficient, it is necessary to carefully select the measured data from which the nine correction parameters are calculated. To obtain reliable parameters,

magnetic measurements are acquired during a calibration manoeuvre, also called figure of merit (FoM), for which the magnetic field has to remain constant as possible (Leliak, 1961); otherwise, Equation (1) is no longer correct and one must take variations of the magnetic field into account. It is therefore necessary to run the FoM over as short a time span as possible. The sensor needs also to browse the broadest range of orientations in the three-dimensional space, as discussed by Munschy et al. (2007). Therefore, using data acquired over some magnetic gradients or not covering enough orientations would lead to useless parameters, unable to correct the entire set of data acquired before or after the calibration manoeuvre.

## CASE STUDIES

### 2022 DETEX2 cruise with NemoSens micro–autonomous underwater vehicle (RTSys)

#### Data acquisition and processing

We illustrate the scalar calibration methodology by a first example of an autonomous underwater vehicle (AUV) trial survey performed by Shom in the shallow waters of the Bay of Brest (Iroise Sea, France, Figure 2) during the DETEX2 cruise in fall 2022. Our goal was to assess the feasibility of working with a small, lightweight and easily deployable AUV for submarine magnetic surveys dedicated to the detection of anthropogenic metallic objects, including unexploded ordnance. We chose to test an about 1.5 m long and less than 10 kg extended version of the NemoSens micro-AUV from the French company RTSys (Figure 3). For our experiment, the payload consisted of positioning, inertial and velocity systems coupled with two long baseline acoustic buoys deployed in the studied area that theoretically offered a positional accuracy of a few meters. An altimeter and a pressure sensor auto-controlled and stabilized the altitude of the vehicle above the sea floor. The AUV was equipped in the front with an Applied Physics Systems 1540 vector fluxgate magnetometer encapsulated in a watertight hull fixed at the end of a rigid pole, as far as possible from electromagnetic noise sources (i.e. engine and propellers at the rear). Note that this experiment, as well as the one described in the '2021 magnetic trial survey with Hugin autonomous underwater vehicle (Kongsberg Discovery)' section, was done after receiving all regulatory approvals from the French maritime authorities and broadcasting emergency alerts for navigators.

The AUV ran several dives, about 3 h each in the estuary of the Aulne River in the Bay of Brest (Figure 2). It was launched with the support of a semi-rigid boat of the hydrographic vessel BH2 Laplace and covers six boxes of interest with areas ranging from 5000 to 80,000 $m^2$. The drone navigated at about three knots, about 3 m above the sea floor, that is very close to anomaly sources. Magnetic data were acquired at 10 Hz along lines with an average spacing of about 5 m. Tie-lines were also measured to estimate differences at crossing points, following Shom's standard acquisition and processing workflow as described by Oehler and Lequentrec-Lalancette (2019).

Figures of merit (FoM) were acquired at the beginning and at the end of each dive to determine calibration coefficients as accurate as possible. The manoeuvre only consisted of flying along two pre-programmed successive circles, the first clockwise and the second counter-clockwise, without any specific actions on pitching and rolling. It allows to cover twice all heading directions and to sample the broadest natural range of attitudes of the AUV. FoMs were measured at a depth of a few metres in just a few minutes. The idea is to avoid significant variations of the magnetic intensity related to local anomalies.

Figure 4 illustrates the flight path of the FoM selected for processing vector data acquired by the AUV in Box 1 and the variations in raw and calibrated total magnetic intensity (TMI), heading, pitch and roll. This FoM was acquired in less than 4 min. Ranges for the attitude of the AUV cover well the parameter space and should provide reliable calibration coefficients. It can be observed that long-wavelength variations of the raw TMI correlate strongly with AUV heading, whereas short-wavelength variations correlate to pitch and roll. The standard deviation between the norms of the raw TMI and the International Geomagnetic Reference Field (IGRF) is about 38.5 nT and is mainly due to static (i.e. remanent and induced) magnetic effects from the AUV's orientation with respect to the Earth's magnetic field. Application of the parameters found by inversion to the FoM shows a dramatic improvement in TMI with a reduction in standard deviation to only 1.7 nT for the calibrated data. In other words, heading effects from the AUV are reduced by 96% of their original value. Consequently, we are confident that these calibration coefficients are suitable for our data set and hence can be applied to the whole survey. The remaining magnetic anomalies are most likely related to seafloor or sub-seafloor sources.

The inverted calibration vector can then be applied to the whole area of interest, here Box 1, following Equation (3). High-frequency variations due to pitch and roll, which are inefficiently corrected by the calibration, are mitigated with a third-order low-pass Butterworth filter with 0.3 or 0.5 Hz cutoff frequency, depending on the frequency range of observed pitch and roll variations during the acquisition. Low-frequency heading residuals are processed by removing the median value for each profile. The same processing workflow was applied for each box by carefully choosing the most appropriate FoM for calibration (i.e. the one minimizing the standard deviation between the norms of the calibrated TMI and the IGRF).

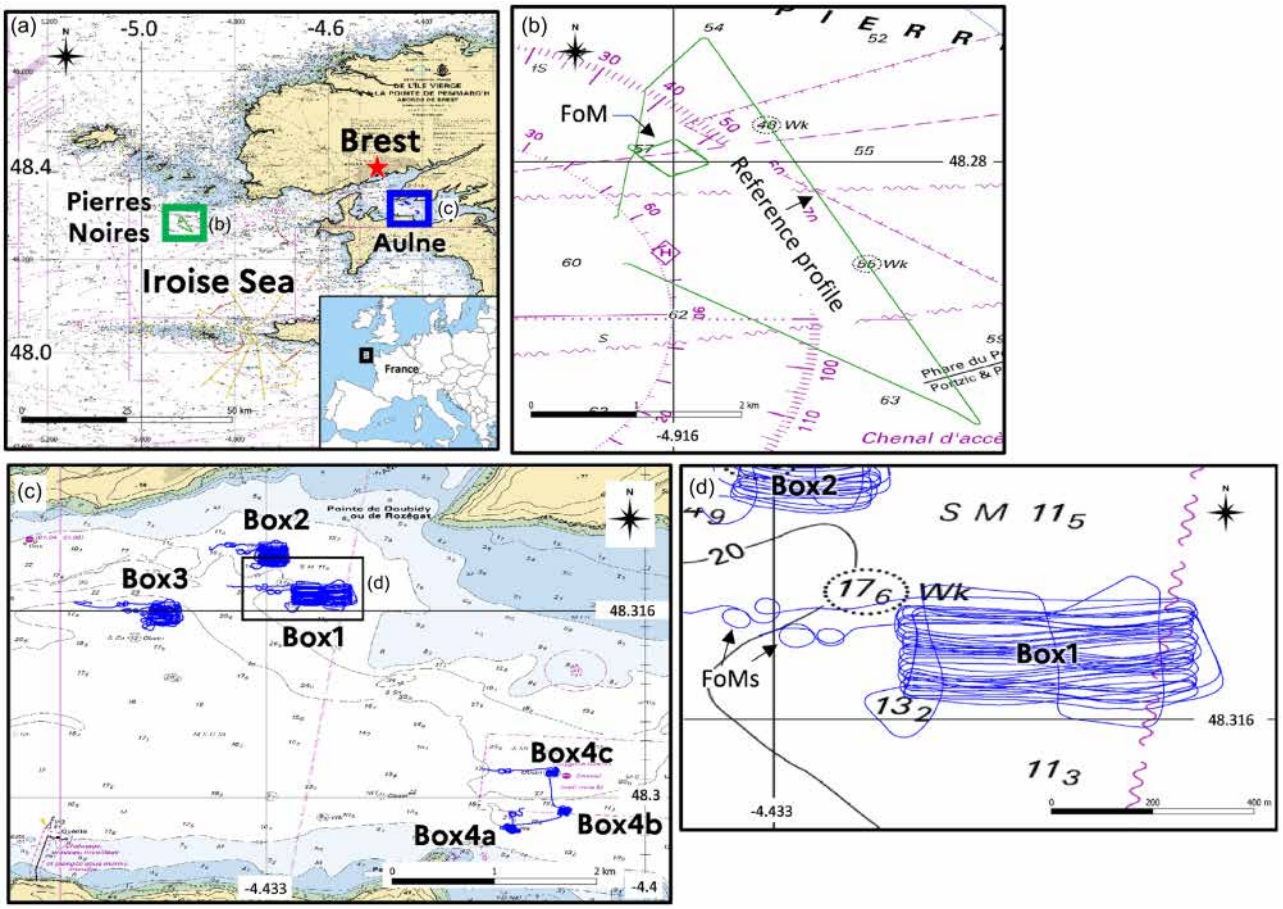


**FIGURE 2** General location maps (a). Tracks of Hugin autonomous underwater vehicle (AUV) (Kongsberg Discovery, in green) during the magnetic trial survey performed in 2021 (b), and tracks of NemoSens AUV (RTSys, in blue) during the magnetic trial survey performed in 2022 (DETEX2 cruise, c and d). Shom's nautical charts are used as background maps.

## Results

We present and interpret results obtained on three of the six surveyed boxes (Boxes 1, 4a and 4b, see Figure 2), as they give a representative overview of the expected performance, and pros and cons of the methodology. They also cover anthropogenic metal objects such as wrecks, obstructions and cables, as well as purposely deployed targets simulating unexploded ordnances (UXOs).

*i. Box 1*

Figure 5A,B shows a comparison between raw and calibrated data for Box 1, along a selected profile and on maps. On the profile, the raw total magnetic intensity (TMI) contains high-frequency noise of several tens of nT. A strong dipolar anomaly of around 700 nT is visible in the centre of the profile. A buried wreck was likely highlighted here. By zooming on the eastern part of the profile, another small anomaly of about 6 nT is visible, but only on the calibrated data. This anomaly coincides with the intersection of a buried communication cable reported in Shom's database (Shom, 2018). The noise level and the static magnetic effects of the autonomous underwater vehicle (AUV) (estimated to be about 40 nT in amplitude, see statistics in Figure 4) hide this anomaly on raw data. This example illustrates the importance of a proper calibration to identify weaker magnetic anomalies below the sea floor, which can best be achieved using vector magnetometers. The raw TMI map is unsurprisingly contaminated by strong profile effects mainly due to the static magnetic signatures of the drone correlated with its heading. On the other hand, the map of calibrated anomalies emphasizes short- and long-wavelength signals by reducing these heading effects. We observe a dramatic improvement in S/N ratio with a residual noise of a few nT that allows the identification of very weak magnetic anomalies. Local anomalies of up to 10 nT are thus interpreted as signatures of small buried objects, considering that the bathymetry of the area is relatively smooth and does not show any evidence of geological or anthropogenic structures. The eastern part of the Box 1 is similarly characterized by a series of aligned dipoles with amplitudes up to tens of nT. This is the signature of the communication cable mentioned above that runs through the Box 1. To be complete,


**FIGURE 3** NemoSens micro-autonomous underwater vehicle (AUV) (RTSys). (a) AUV ready to dive in front of BH2 Laplace vessel. (b) Launch from the rear platform deck of the hydrographic launch. (c) Watertight hull encapsulating the Applied Physics Systems 1540 vector fluxgate magnetometer tied to the AUV by a pole.

an anomaly of about 300 nT is visible after calibration in the south-east of the box and is likely related to a large buried object or a wreck. The long-wavelength anomaly observed across the Box 1 probably has a geological origin.

*ii. Box 4a*

Figure 6A,B illustrates results for Box 4a. Again, raw TMI is noisy with strong effects due to the static magnetic signatures of the drone. The calibration efficiently corrects heading as well as at least partially pitch effects. It allows for a clear identification of a magnetic dipole of about 40 nT in amplitude, which was not visible on raw TMI data. The wreck of a small plane is known to be located in this area with a 10 m uncertainty on its position (Shom, 2022). The highlighted magnetic anomaly is therefore related to this object but seems slightly shifted to the north-east. We conclude that the position of the wreck needs to be corrected, even if the positioning of the drone also appears to show some inaccuracy. An alternative interpretation is that we measured the signature of other parts of the plane wreck.

*iii. Box 4b*

Figure 7A,B illustrates results for Box 4b. As usual, raw TMI shows profile effects and calibrated data allow the identification of several small magnetic anomalies of several tens of nT and clearly weaker than the noise level of raw data. Here the dipole anomalies are the magnetic signatures of purposely dropped steel targets simulating UXOs. However, just like for Box 4a, anomalies are shifted compared to the expected positions of the targets. It can be explained by either the inaccurate navigation of the AUV or a possible displacement of the targets in this sector of the Bay of Brest where hydrodynamics are strong.

## 2021 magnetic trial survey with Hugin autonomous underwater vehicle (Kongsberg Discovery)

The second example presents magnetic data acquired during a Shom's trial survey in fall 2021 with a 3-axis Ocean Floor Geophysics Self-Compensating Magnetometer (OFG-SCM) embedded in the 6.6 m long and 2200 kg Hugin 6000 Superior AUV (Kongsberg Discovery). The scalar calibration is applied to a data subset from the Pierres Noires area (Iroise Sea, France), 50 km to the West of Brest, where a scalar magnetic reference profile has been acquired by Shom for research and calibration purposes (Figure 2). Magnetic data

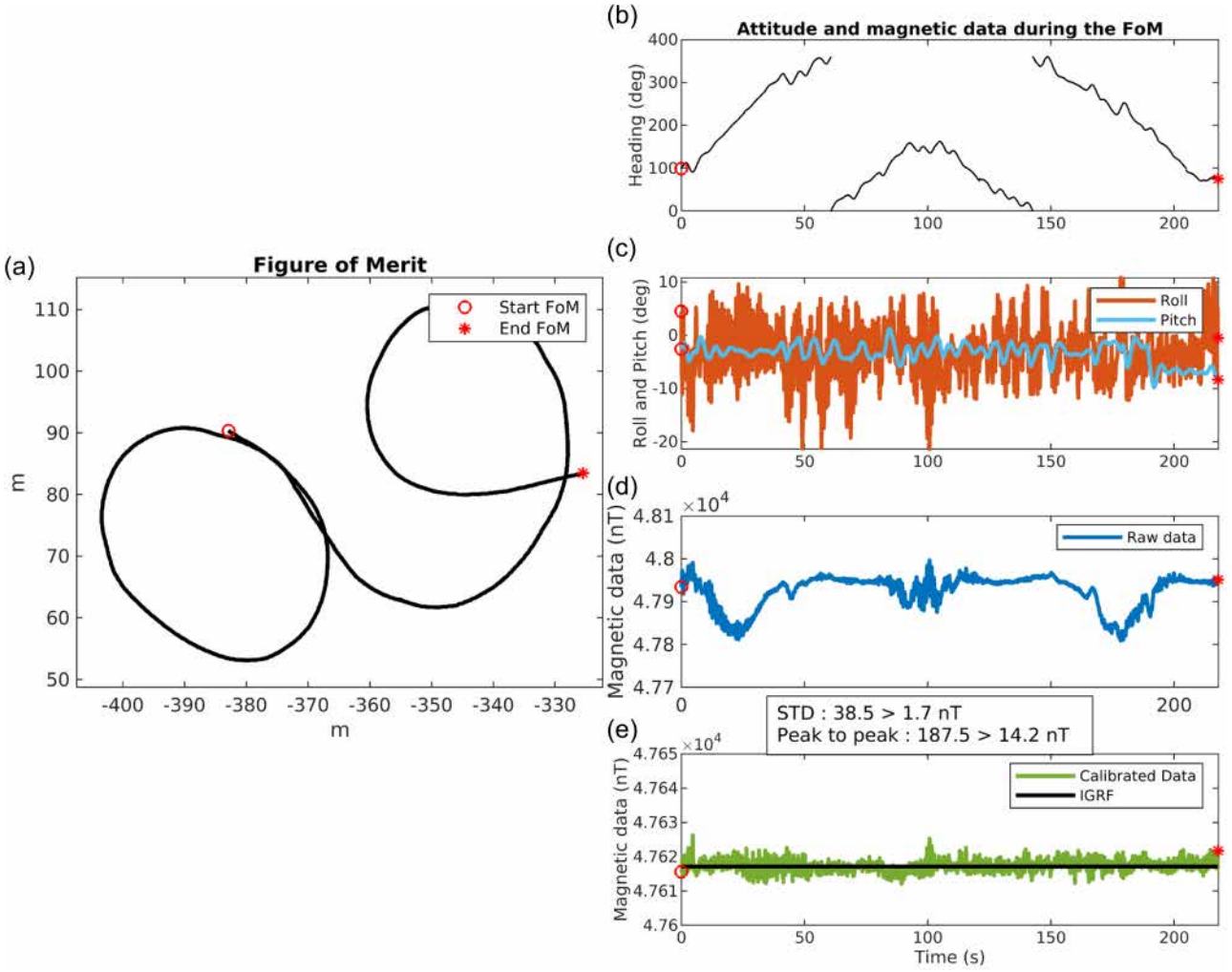


**FIGURE 4** Path of a figure of merit (FoM) of NemoSens autonomous underwater vehicle (AUV) (a). Time series of drone heading (b) and pitch and roll (c), and raw (d) and calibrated (e) magnetic data. Intensities of the magnetic data are given in nT, heading, roll and pitch angles in degrees. The standard deviation between the norms of the raw total magnetic intensity (TMI) and the International Geomagnetic Reference Field (IGRF) is about 38.5 nT and is reduced to only 1.7 nT for the calibrated data. Peak-to-peak ranges similarly decrease from 187.5 nT before calibration to 14.2 nT after. STD, standard deviation of differences. *Source*: IGRF data are from Alken et al. (2021).

were recorded at 20 Hz together with positioning and attitude data at 100 Hz along with a whole array of hydrographic and oceanographic measurements. Here we obviously focus on magnetometry and attitude. The goal is to apply our processing workflow to evaluate its efficiency in correcting the static magnetic effects of a much larger AUV.

Figure 8 illustrates the flight path of the figure of merit (FoM) for the processing of OFG-SCM data and the corresponding variations in raw and calibrated TMI, heading, pitch, roll and depth of the drone. The FoM consisted in the two sequential coincident squares already described by Bloomer et al. (2014). It was acquired in about 25 min over a 7000 $m^2$ area. The AUV cyclically dove and went up on about 20 m depth during the FoM. It consequently led to a more complete coverage of parameter space with variations in pitch to $\pm 20^{\circ}$ – for comparison, the range of values for NemoSens AUV was only a few degrees (Figure 4). Here, we observe a good correlation between long-wavelength variations of the raw TMI and the AUV heading and pitch. Short-wavelength variations seem more likely due to roll. The standard deviation of the difference between the norms of the raw TMI and the International Geomagnetic Reference Field (IGRF) is about 118.2 nT, that is the static magnetic effects from Hugin AUV are about three times greater than those from NemoSens AUV. This standard deviation for the calibrated TMI after processing decreases to 6.0 nT, that is heading and pitch effects from the AUV are reduced by 95% of their original value.

Calibration parameters and the same processing workflow as before were then applied to the raw TMI data measured about 10 m above the seafloor on Shom's reference profile. Processed vector data were upward continued to be compared with scalar magnetic data previously acquired at sea

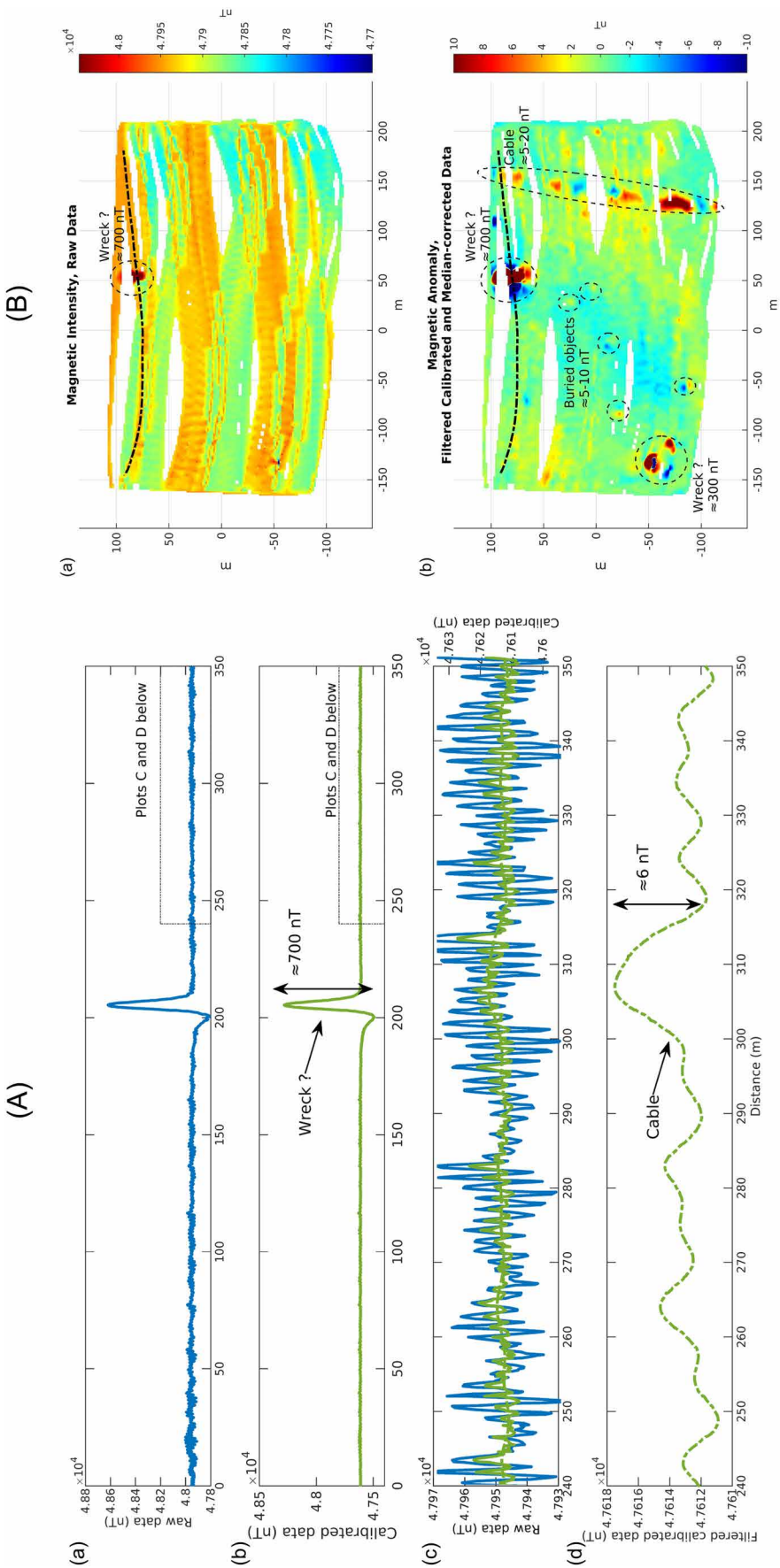


**FIGURE 5** (A) Results for Box 1. Raw total magnetic intensity (TMI, a), calibrated TMI (b) and zoom on raw and calibrated TMI (c and d) for a selected profile (black dashed line in B). (B) Raw (a) and calibrated (b) total magnetic intensity (TMI) maps drawn from 1.5-m gridded model calculated with a triangulation-based natural neighbour interpolation. Note that extreme values in colour bars are saturated.

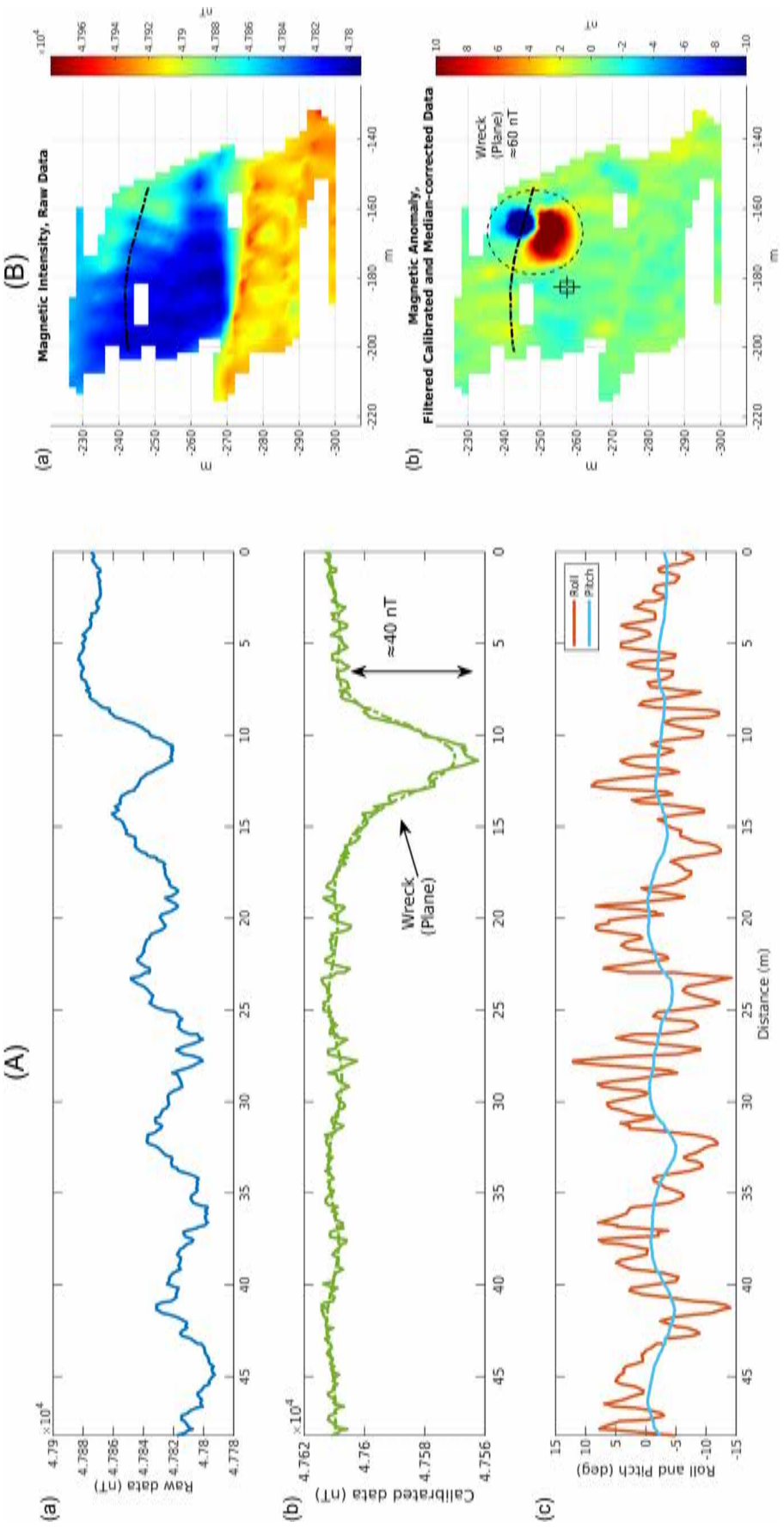


**FIGURE 6** (A) Results for Box 4a. Raw total magnetic intensity (TMI, a), calibrated TMI (b) and attitude data (c) for a selected profile (black dashed line in B). (B) Raw (a) and calibrated (b) total magnetic intensity (TMI) maps drawn from 1.5-m gridded model calculated with a triangulation-based natural neighbour interpolation. Note that extreme values in colour bars are saturated. The target symbol gives the known location of the wreck of a plane (Shom, 2022).

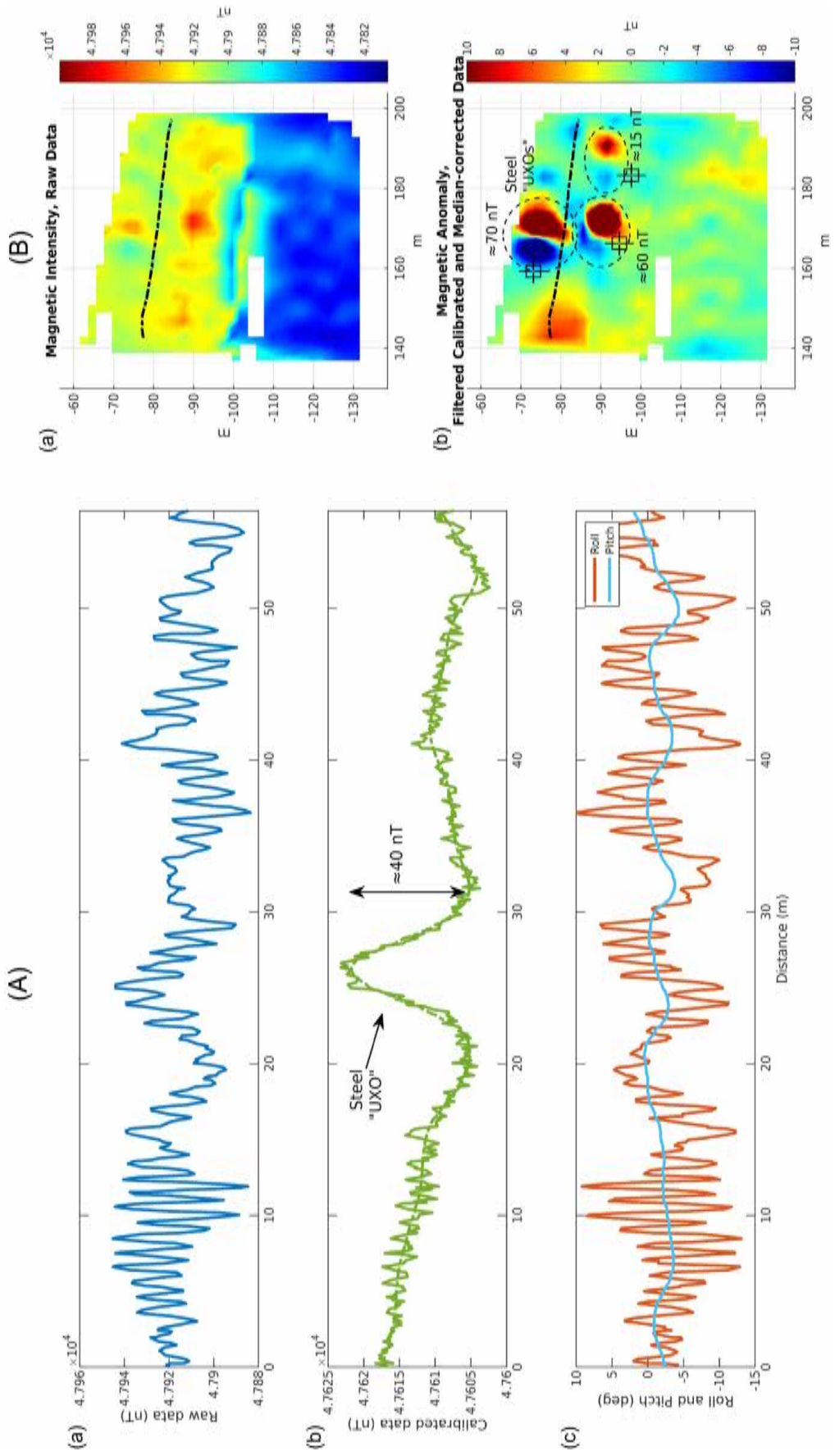


**FIGURE 7** (A) Results for Box 4b. Raw total magnetic intensity (TMI, a), calibrated TMI (b) and attitude data (c) for a selected profile (black dashed line in B). UXO, unexploded ordnance. (B) Raw (a) and calibrated (b) total magnetic intensity (TMI) maps drawn from 1.5-m gridded model calculated with a triangulation-based natural neighbour interpolation. Note that extreme values in colour bars are saturated. The target symbols give the location of purposely buried steel targets simulating unexploded ordnances (UXOs).

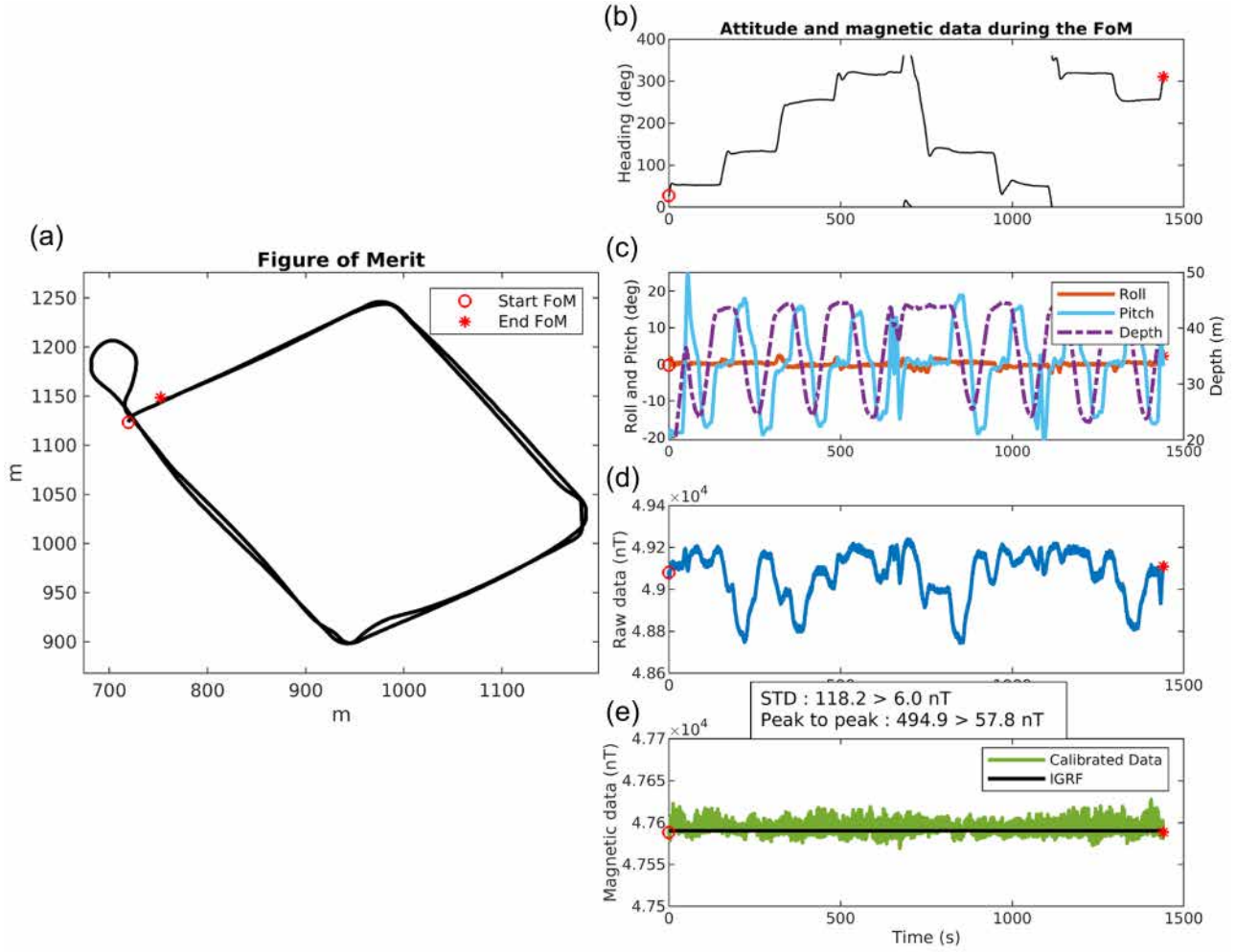


**FIGURE 8** Path of a figure of merit of Hugin autonomous underwater vehicle (AUV) (a). Time series of drone heading (b) and depth, pitch and roll (c), and raw (d) and calibrated (e) magnetic data. Intensities of the magnetic data are given in nT; heading, roll and pitch angles in degrees and depth in metres. The standard deviation between the norms of the raw total magnetic intensity (TMI) and the International Geomagnetic Reference Field (IGRF) is 118.2 nT and is reduced to only 6.0 nT for the calibrated data. Peak to peak ranges similarly decrease from 494.9 nT before calibration to 57.8 nT after. STD, standard deviation of differences. *Source*: IGRF data are from Alken et al. (2021).

level with a towed system that we consider here as a benchmark. Results are shown in Figure 9. Obviously, no calibration would be needed as the static effects of the drone are negligible with regard to the >2500 nT peak-to-peak magnetic dipole associated with the well-known shipwreck of the 120 m-long *Katingo* cargo (Shom, 2022). However, the calibration procedure clearly improves the quality of AUV vector data by partially removing parasite signals due to pitch variations.

For example, to the north-east of the profile (to the left), an about 150 nT pitch effect is dramatically reduced to a few tens of nT in the calibrated data. In the central part (around 2400 m, to the right), a longer wavelength anomaly interpreted to be of geological origin is similarly filtered from noise of about 200 nT peak-to-peak corresponding to noticeable variations in pitch. We note that raw and calibrated TMI remains noisy with high frequencies of several tens of nT in amplitude. This noise is the combination of imperfect corrections of pitch and roll effects and of other electromagnetic perturbations and needs to be filtered with a low-pass filter, just as we did for the NemoSens AUV. Upward-continued AUV data are in good agreement with scalar reference data measured at sea level. Data acquired with the AUV are very close to the seafloor and provide higher resolution of signal from small sources.

## 2021 RR2102 cruise with Sentry autonomous underwater vehicle (Woods Hole Oceanographic Institution)

As a last example, we downloaded open-access data from the 2021 RR2102 cruise performed with Sentry AUV from Woods Hole Oceanographic Institution along the East Pacific Rise Axis (Parnell-Turner et al., 2023). The aim is to

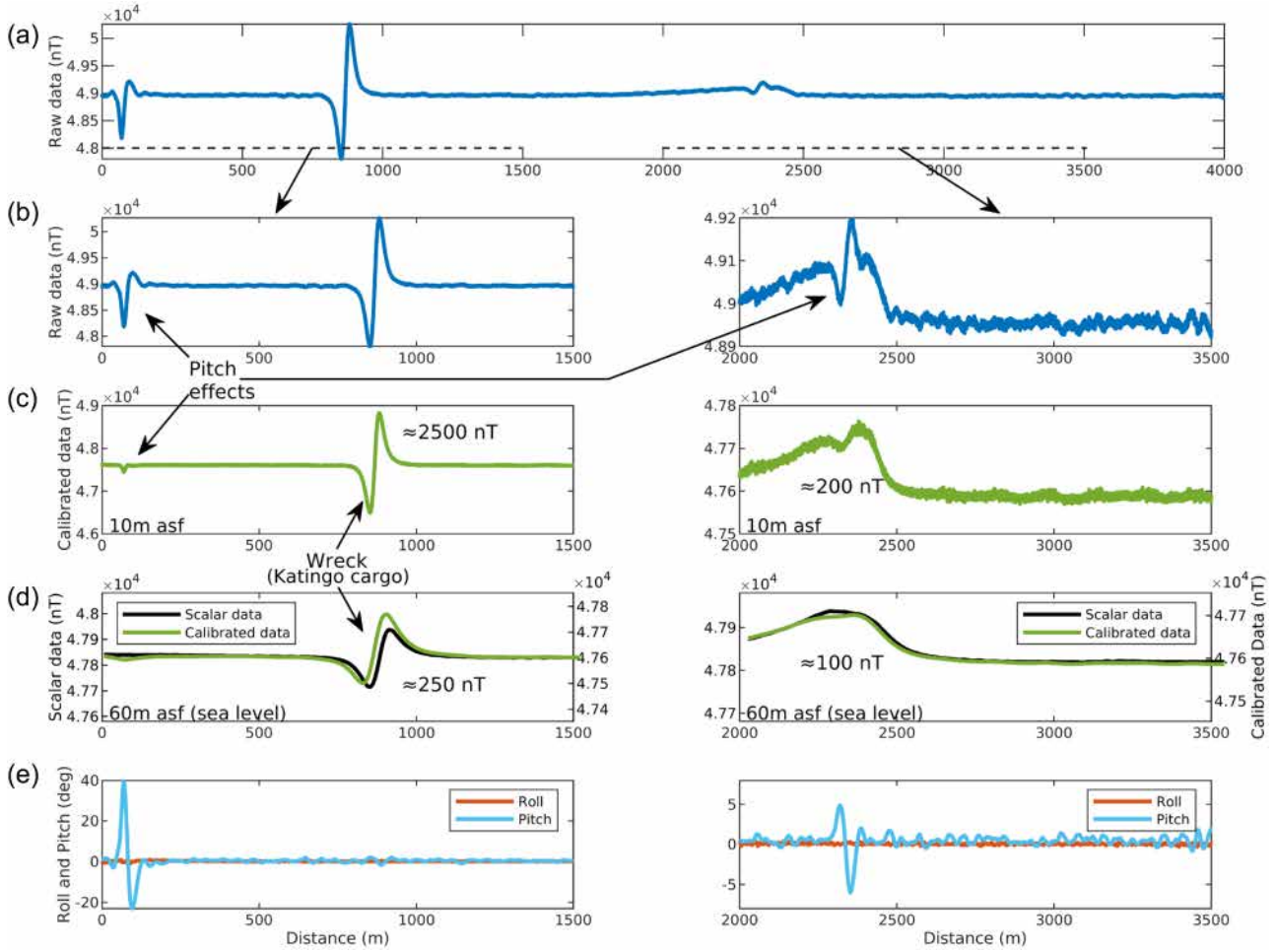


**FIGURE 9** Application to Hugin autonomous underwater vehicle (AUV). Raw total magnetic intensity (TMI) on Shom's magnetic reference profile in the Pierres Noires area (a, see location in Figure 2) and zooms on two specific sections. Note that vertical scales are different. From top to bottom, raw TMI (b), calibrated TMI (c) at the altitude of the drone (i.e. 10 m above the sea floor), upward-continued calibrated TMI and scalar reference data at the sea level (d) and attitude data (e).

demonstrate that our workflow can be applied to different types of sensors and systems. Sentry AUV is intermediate in size between NemoSens and Hugin (i.e. 1.8 m in height, 2.2 m wide including thrusters and 2.9 m long). Following Berrios-Rivera et al. (2023), we worked only with data from the Applied Physics System Model 1520 triaxial fluxgate magnetometer mounted near the top of the AUV. We selected from data a specific navigation spin of Sentry typically used for calibration of magnetic data and used it as a FoM (Figure 10). The spin was performed in about 4 min, at a depth of around 2583 m. The flight path is narrow and laterally spreads on less than 20 m. On the one hand, the range of heading values is complete and even oversampled. On the other hand, variations in pitch and roll are only of a few degrees. Thus, long-wavelength variations of the raw TMI are strongly linked to variations of the AUV heading. The standard deviation of the difference between the norms of the raw TMI and the IGRF is about 97.3 nT. After inversion, it decreases to 5.8 nT; in other words, we achieve the reduction of 94% of the original noise. We are therefore confident that heading effects from the Sentry AUV are almost completely reduced, as for the previous examples.

## DISCUSSION

Results presented here and synthesized in Table 1 suggest that a simple optimized scalar calibration method derived from aeromagnetic and satellite applications (Munschy et al., 2007; Olsen et al., 2003) is quite efficient to reduce the static magnetic signature of autonomous underwater vehicles (AUVs): mainly the induced field due to their orientation in the Earth's magnetic field and the permanent field due to their steel structure and their payload. Calibration residuals that predominantly consist of poorly compensated heading effects are only simply processed by removing a median value per profile and do not need heading tests. This process also filters out tide issues in shallow waters and diurnal variations of the Earth's

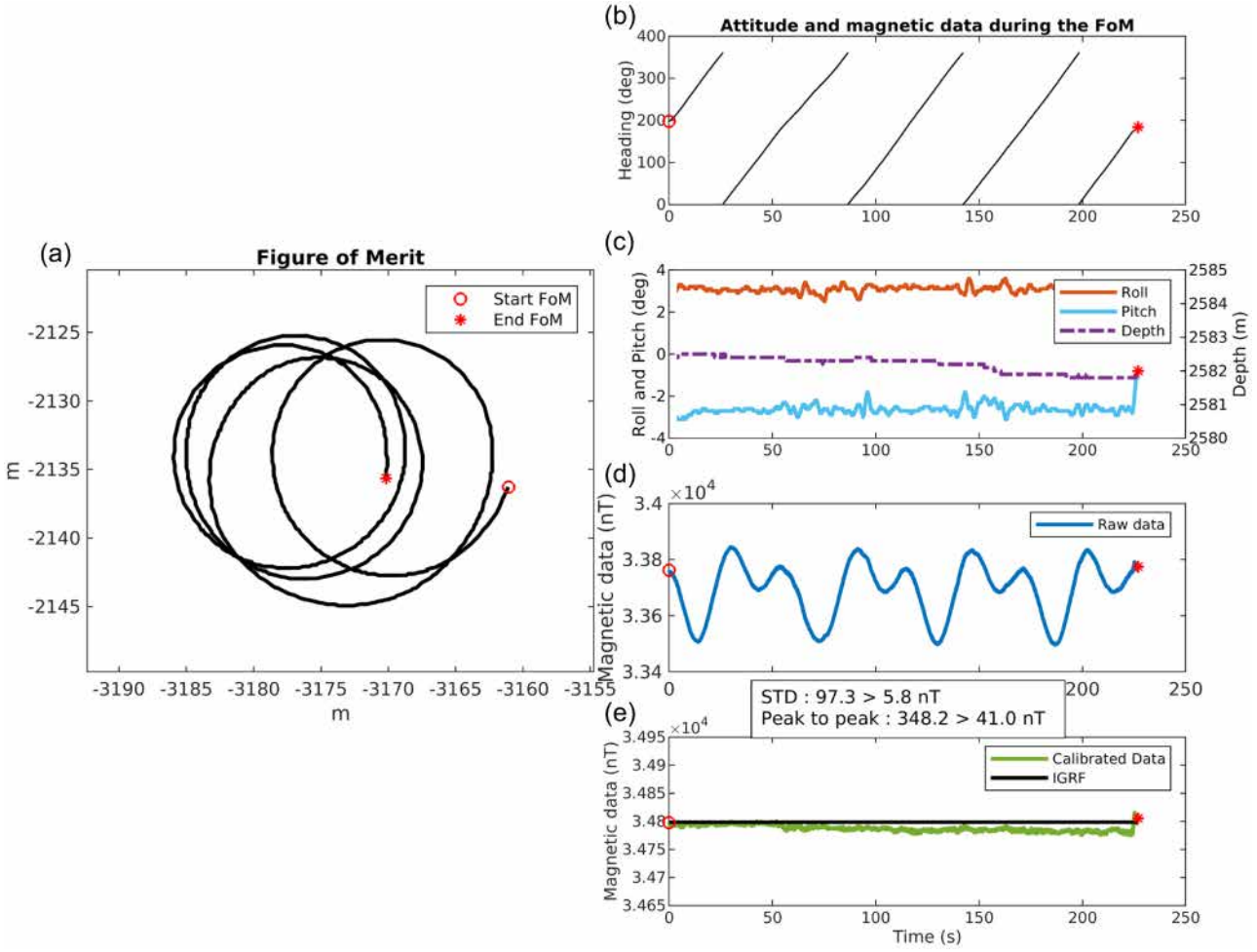


**FIGURE 10** Path of a figure of merit of Sentry autonomous underwater vehicle (AUV) (a). Time series of drone heading (b) and depth, pitch and roll (c), and raw (d) and calibrated (e) magnetic data. Intensities of the magnetic data are given in nT, heading, roll and pitch angles in degrees and depth in metres. The standard deviation between the norms of the raw total magnetic intensity (TMI) and the International Geomagnetic Reference Field (IGRF) is 97.3 nT and is reduced to only 5.8 nT for the calibrated data. Peak-to-peak ranges similarly decrease from 348.2 nT before calibration to 41.0 nT after. STD, standard deviation of differences. *Source*: IGRF data are from Alken et al. (2021).

magnetic field if the survey is short in duration as was the case here for the NemoSens AUV.

Induced magnetic fields from eddy currents are neglected or considered to be part of the measurement noise. Applying a low-pass filter after calibration at least partially removes this signal, as well as the high-frequency residual variations due to pitch and roll. We, however, have to keep in mind that a true signal can also be filtered out if signal and noise have similar frequency ranges. The processing workflow applied to magnetic data acquired with the three selected AUVs of increasing sizes gives reliable results as it validates that an accurate measurement can be made. Even magnetic anomalies of a few nT can be detected and mapped with NemoSens AUV.

Expected sensitivities for the larger Sentry and Hugin AUVs are one order of magnitude larger, mainly because of the stronger heading effects, thus lower S/N ratios. The uncertainty analysis conducted on the raw and processed total magnetic intensity (TMI) data acquired by NemoSens AUV also emphasizes the advantages of a proper calibration (Table 2). Errors for raw TMI data in the three Boxes are statistically estimated to be about 40 nT respectively, whereas they decrease to less than 10 nT for calibrated and filtered TMI data.

The position and the type of embedded magnetic sensors are more critical to the magnetic data quality than the size of the AUV, even though it is more challenging to mitigate the magnetic noise produced by a larger carrier. As stated earlier, manufacturers chose to mount the magnetometer on a front pole inside the NemoSens AUV and on the top of Sentry AUV to locate the sensor as far as possible from the electromagnetic noise of the drone due to engines, thrusters, batteries or other sensors. In addition and as shown in Equation (1), it is required to measure the three components of the Earth's magnetic field to have access to the nine parameters allowing the

**TABLE 1** Synthesized view of the main results of this study.

| AUV | NemoSens (RTSys) | Sentry (WHOI) | Hugin Superior 6000 (Kongsberg Discovery) |
|---|---|---|---|
| Size | Small-sized AUV (micro-AUV) | Intermediate-sized AUV | Large-sized AUV |
| Magnetic sensor | Embedded<br>3-axis fluxgate<br>APS 1540 | Embedded<br>3-axis fluxgate<br>APS 1520 | Embedded<br>3-axis fluxgate<br>OFG-SCM |
| Processing | Scalar calibration | | |
| FoM | Figure 8 type at constant altitude | Several spins at constant altitude | 2 sequential coincident squares with dives |
| Max. heading effect before/after calibration (nT) | 190 → 14 | 350 → 40 | 500 → 60 |
| STD (vs. IGRF) before/after calibration (nT) | 40 → 2 | 100 → 6 | 120 → 6 |
| Detection threshold (sensitivity) | A few nT | Tens of nT | Tens of nT |

*Note*: STD is standard deviation of differences.
Abbreviations: AUV, autonomous underwater vehicle; FoM, figure of merit; IGRF, International Geomagnetic Reference Field; nT, nanoTeslas; OFG-SCM, Ocean Floor Geophysics Self-Compensating Magnetometer; WHOI, Woods Hole Oceanographic Institution.

**TABLE 2** Uncertainty analysis from statistics on differences at crossing points for raw and processed total magnetic intensity (TMI) data on Box 1 and Boxes 4a and 4b taken together.

| | | STD (nT) | Max. differences (nT) | Number of crossing points |
|---|---|---|---|---|
| Box 1 | Raw TMI | 35.2 | ±98.7 | 402 |
| | Calibrated TMI | 8.0 | ±25.6 | |
| | Calibrated and filtered TMI | 7.5 | ±19.8 | |
| Boxes 4a+4b | Raw TMI | 42.4 | ±105.2 | 38 |
| | Calibrated TMI | 5.1 | ±19.9 | |
| | Calibrated and filtered TMI | 4.1 | ±19.1 | |

*Note*: STD is standard deviation of differences.
Abbreviation: nT, nanoTeslas.

correction of both the defaults of the fluxgate magnetometer and the static magnetic signature of the carrier (Munschy et al., 2007). It is therefore essential to work with a properly integrated vector magnetometer.

The method moreover needs calibration manoeuvres to be successful. Our case studies illustrate three different kinds of figure of merits (FoMs): Figure 8 navigation paths, several spins or coincident squares with or without variations in depths. For all of them, the main goal is to sample the widest range of the AUV's heading and attitude (in heave, roll and pitch) as possible and to understand how they perturb the magnetic measurements, under the assumption that we have a known and constant regional magnetic field at the FoM location. Hence, FoMs have relatively small spatial footprints and try to avoid areas with strong lateral gradients. Even if the FoMs are quite different in shapes, durations and in the ways of being acquired, their most important common features are the complete coverage and even the oversampling of heading directions. This information is necessary to accurately correct the profile effects due to the rotation of the drone in the ambient magnetic field. Values of roll and pitch during the FoMs vary sharply according to the AUV, which also provides information on the diving behaviour of the drone. Although the Sentry AUV is relatively stable with variations in pitch and roll smaller than 1°, the NemoSens AUV has strong variations in roll (about 30°) and the Hugin AUV in pitch (more than 40°) correlated with its successive dives. It is clear from the example of the Hugin AUV measuring on Shom's reference profile that pitch effects are also at least partially corrected after calibration. We are therefore confident that significant variations in pitch and roll help to yield better calibration parameters.

A total of eight Figure 8 type FoMs were performed during the NemoSens AUV trial survey, one at the beginning and one at the end of each dive (Figure 2). They give access to a rich database of the nine calibration parameters of offset, sensitivity and angle. Results are graphically synthesized

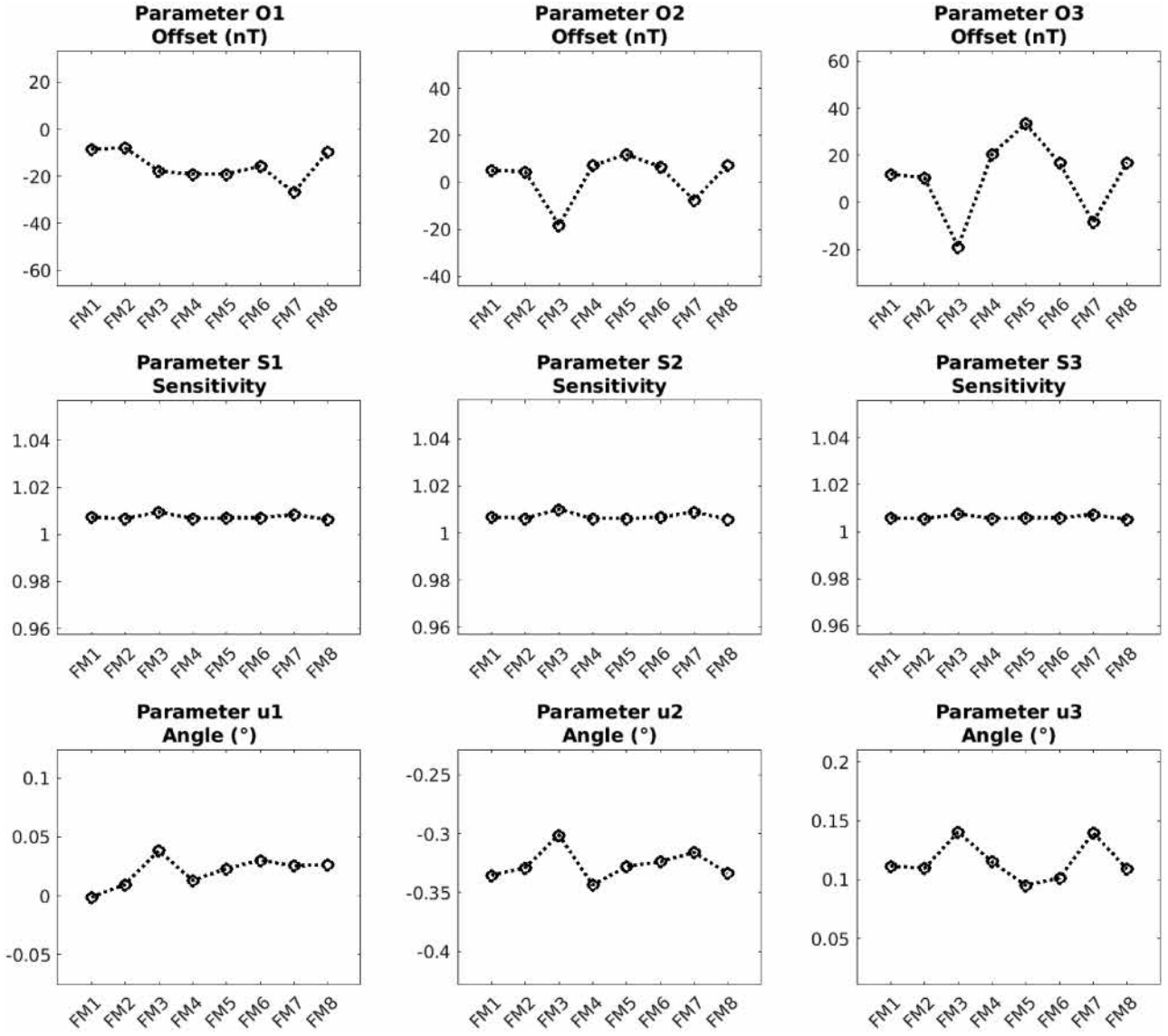


**FIGURE 11** Calibration parameters of offset, sensitivity and angle calculated by inversion from the eight figures of merit (FoM) measured during NemoSens autonomous underwater vehicle (AUV) tests.

in Figure 11. Industry specifications give errors smaller than 13 nT in offset (estimated at about 12°C, that is the average sea water temperature during the survey) and smaller than 0.2° in angle for APS1540 magnetometer sensor (Applied Physics Systems, 2022). Our calibration results show offsets of several tens of nT and angles $u_2$ exceeding 0.3°. These values are interpreted as the AUV magnetic footprint, confirming that the calibration is useful to correct not only the sensor's imperfections but also the carrier effects. Repeating the FoM moreover allows to study of the stability of the calibration parameters over the whole duration of the survey without any changes in the carrier set-up. The plots in Figure 11 confirm that the calibration parameters are quite stable for most FoMs, except for FoMs 3 and 7 where significant variations in offsets and angles are observed. We are not able yet to explain why these particular FoMs give distinct parameters. The only differences between FoMs concern the location and date of their acquisition leading to potential differences in amplitudes due to external variations of the Earth's magnetic field, tide variations or local geological gradients. Here, FoMs 3 and 7 were discarded for the calibration of NemoSens AUV data. This analysis also consequently shows that the preferable option is to schedule several FoMs during a survey to ensure at least some valuable manoeuvres.

## CONCLUSIONS

Performing underwater magnetic surveys with embedded sensors on autonomous underwater vehicles (AUVs) is the most practical way to acquire data very close to sources and optimize their detection and mapping, even in deep waters (here to

2500 m in depth for Sentry AUV and announced to be more for Hugin, per its manufacturer). To ensure success, a careful integration study of the magnetic sensor is needed, a 3-axis vector magnetometer is necessary and a simple optimized scalar calibration with the acquisition of specific figures of merit is sufficient to mitigate the main part of the static magnetic signature of the drone. Calibration residuals are removed by additional processing such as the removal of a median value per profile and low-pass filtering. Results are impressive and show that even weak magnetic anomalies smaller than 10 nT can be highlighted, even though the magnetic signatures of AUVs can be orders of magnitude higher.

## ACKNOWLEDGEMENTS

This study was carried out as part of the research contract MAGIDRO between ITES and Shom. MAGIDRO is funded by the Defence Innovation Agency (DIA), French Ministry for Armed Forces, through the Defence Technologies Project APOGé led by Shom. Special thanks are sent to the crew of BH2 Laplace and BHO Beautemps-Beaupré, Shom's hydrographers and drone experts at RTSys and Kongsberg Discovery. Steel targets were purposely dropped in the Bay of Brest by French Defence Procurement Agency (DGA-TN Brest). 2021 Hugin AUV trials were funded by the French Defence Procurement Agency (DGA) as part of the preparatory phase for the replacement of the hydro-oceanographic fleet (CHOF project). Near-bottom Sentry AUV raw magnetic data collected during RR2102 survey (Parnell-Turner et al., 2023) were downloaded from Marine Geoscience Data System (MGDS) website (www.marine-geo.org).

## FUNDING INFORMATION

The research contract MAGIDRO is funded by the Defence Innovation Agency (DIA), French Ministry for Armed Forces, through the Defence Technologies Project APOGé led by Shom. 2021 Hugin AUV trials were moreover funded by the French Defence Procurement Agency (DGA) as part of the preparatory phase for the replacement of the hydro-oceanographic fleet (CHOF project).

## DATA AVAILABILITY STATEMENT

NemoSens and Hugin data are proprietary and cannot be released. Sentry data (Parnell-Turner et al., 2023) can be freely downloaded from MGDS website (www.marine-geo.org).

## ORCID

*J.-F. Oehler* https://orcid.org/0000-0002-3197-2465
*G. Marquis* https://orcid.org/0000-0001-8971-6846

## REFERENCES

Alken, P., Thébault, E., Beggan, C.D., Aubert, J., Baerenzung, J., Brown, W.J. et al. (2021) Evaluation of candidate models for the 13th generation International Geomagnetic Reference Field. *Earth Planets and Space*, 73, 48. Available from: https://doi.org/10.1186/s40623-020-01281-4

Applied Physics Systems. (2022) *MODEL 1540 magnetometer sensor*. Available at: https://appliedphysics.com/wp-content/uploads/2023/09/Model1540_DEF_DataSheet_vA.pdf

Berrios-Rivera, N., Gee, J.S., Parnell-Turner, R., Maher, S., Wu, J.-N., Fornari, D. et al.(2023) Significance of short-wavelength magnetic anomaly low along the East Pacific Rise axis, 9°50′N. *Geochemistry, Geophysics, Geosystems*, 24, e2023GC010875. Available from: https://doi.org/10.1029/2023GC010875

Bloomer, S., Kowalczyk, P., Williams, V., Wass, T. & Enmoto, K. (2014) Compensation of magnetic data for autonomous underwater vehicle mapping surveys. 2014 IEEE/OES *autonomous underwater vehicles* (AUV). New York City, IEEE. pp. 1–4. Available from: https://doi.org/10.1109/AUV.2014.7054417

Dhanak, M., An, E., Couson, R., Frankenfield, J., von Ellenrieder, K. & Venezia, W. (2013) Magnetic field surveys of coastal waters using an AUV-towed magnetometer. 2013 OCEANS—San Diego, *San Diego, CA, USA*. New York City, IEEE. pp. 1–4. Available from: https://doi.org/10.23919/OCEANS.2013.6741358

Faramarzi, A., Heidarinejad, M., Mirjalili, S. & Gandomi, A.H. (2020) Marine predators algorithm: a nature-inspired metaheuristic. *Expert Systems with Applications*, 152, 113377. Available from: https://doi.org/10.1016/j.eswa.2020.113377

Gallimore, E., Terrill, E., Pietruszka, A., Gee, J., Nager, A. & Hess, R. (2020) Magnetic survey and autonomous target reacquisition with a scalar magnetometer on a small AUV. *Journal of Field Robotics*, 37, 1246–1266. Available from: https://doi.org/10.1002/rob.21955

Guo, C., Zhang, X., Wang, D., Shen, C. & Zeng, F. (2022) Adaptive calibration of the rotation error of total magnetic field for AUV based on marine predators algorithm. 2022 WRC Symposium on Advanced Robotics and Automation, Beijing, China. New York City, IEEE. pp. 77–83. Available from: https://10.1109/WRCSARA57040.2022.9903980

Honsho, C., Ura, T. & Kim, K. (2013) Deep-sea magnetic vector anomalies over the Hakurei hydrothermal field and the Bayonnaise knoll caldera, Izu-Ogasawara arc, Japan. *Journal of Geophysical Research: Solid Earth*, 118. 5147–5164. Available from: https://doi.org/10.1002/jgrb.50382

Isezaki, N. (1986) A new shipboard three-component magnetometer. *GEOPHYSICS*, 51(10), 1992–1998. https://doi.org/10.1190/1.1442054

Kasaya, T., Nogi, Y. & Kitada, K. (2023) Advanced magnetic survey system and method for detailed magnetic field mapping near the sea bottom using an autonomous underwater vehicle. *Exploration Geophysics*, 54(2), 205–216. Available from: https://doi.org/10.1080/08123985.2022.2089013

Leliak, P. (1961) Identification and evaluation of magnetic-field sources of magnetic airborne detector equipped aircraft. *IRE Transactions on Aerospace and Navigational Electronics*, ANE-8, 95–105. Available from: https://doi.org/10.1109/TANE3.1961.4201799

Munschy, M., Boulanger, D., Ulrich, P. & Bouiflane, M. (2007) Magnetic mapping for the detection and characterization of UXO: use of multi-sensor fluxgate 3-axis magnetometers and methods of interpretation. *Journal of Applied Geophysics*, 61, 168–183. Available from: https://doi.org/10.1016/j.jappgeo.2006.06.004

Oehler, J.-F. & Lequentrec-Lalancette, M.-F. (2019) The contribution of marine magnetics in the Gulf of Saint-Malo (Brittany, France) to the understanding of the geology of the North Armorican Cadomian belt.

*Comptes Rendus Geoscience*, 351(1), 1–9. Available from: https://doi.org/10.1016/j.crte.2018.10.002

Olsen, N., Tøffner-Clausen, L., Sabaka, T.J., Brauer, P., Merayo, J.M.G., Jørgensen, J.L. et al. (2003) Calibration of the Ørsted vector magnetometer. *Earth Planets and Space*, 55, 11–18. Available from: https://doi.org/10.1186/BF03352458

Parnell-Turner, R., Gee, J., Berrios-Rivera, N., Fornari, D., McDermott, J. & Barreyre, T. (2023) *Near-bottom AUV Sentry raw magnetic data (ASCII format) from 9°50′N, East Pacific Rise (2021, RR2102)*. IEDA. Available from: https://doi.org/10.26022/IEDA/331249

Primdahl, F. (1979) The fluxgate magnetometer. *Journal of Physics E: Scientific Instruments*, 12, 241. Available from: https://doi.org/10.1088/0022-3735/12/4/001

Seidel, M., Frey, T. & Greinert, J. (2023) Underwater UXO detection using magnetometry on hovering AUVs. *Journal of Field Robotics*, 40, 848–861. Available from: https://doi.org/10.1002/rob.22159

Shom. (2018) *Submarine cables and pipelines*. Available at https://diffusion.shom.fr/donnees/base-de-donnees-maritimes-et-littorales/cables.html

Shom. (2022) *Wrecks and obstructions*. Available at https://diffusion.shom.fr/donnees/base-de-donnees-maritimes-et-littorales/epaves.html

Teixeira, F.C., Quintas, J. & Pascoal, A. (2016) Experimental validation of magnetic navigation of marine robotic vehicles. *IFAC-PapersOnLine*, 49(23), 273–278.

Tilley, D., Dhanak, M., An, E. & Von Ellenrieder, K. (2012) Characterizing magnetic sensors and magnetic noise of AUVs. 2012 Oceans, *Hampton Roads, VA, USA*. New York City, IEEE. pp. 1–5. Available from: https://doi.org/10.1109/OCEANS.2012.6404990

Tivey, M.A., Johnson, H.P., Bradley, A. & Yoerger, D. (1998) Thickness of a submarine lava flow determined from near-bottom magnetic field mapping by autonomous underwater vehicle. *Geophysical Research Letters*, 25, 805–808. Available from: https://doi.org/10.1029/98GL00442

Wang, Z., Liu, S., Guo, Y., Wu, Y. & Wang, Y. (2023) Underwater multi-parameter magnetic anomaly detection system carried by autonomous underwater vehicle and its data preprocessing method. *IEEE 16th International conference on electronic measurement & instruments (ICEMI), Harbin, China*. New York City, IEEE. pp. 280–285. Available from: https://10.1109/ICEMI59194.2023.10270437

**How to cite this article:** Oehler, J.-F., Schifano, V., Marquis, G., Reiller, H., Lucas, S. & Bougeault, C. (2024) Processing of unmanned underwater vehicle vector magnetometer data. *Geophysical Prospecting*, 1–17. https://doi.org/10.1111/1365-2478.13556